An investigation of the thermo-mechanical features of Laohugou Glacier No.12 in Mt. Qilian Shan, western China, using a two-dimensional first-order flow-band ice flow model

Yuzhe Wang[1,2], Tong Zhang[3,1], Jiawen Ren[1], Xiang Qin[1], Yushuo Liu[1], Weijun Sun[4], Jizu Chen[1,2], Minghu Ding[3], Wentao Du[1,2], and Dahe Qin[1]

[1]State Key Laboratory of Cryospheric Sciences, Cold and Arid Regions Environmental and Engineering Research Institute, Chinese Academy of Sciences, Lanzhou 730000, China
[2]University of Chinese Academy of Sciences, Beijing 100049, China
[3]Insititue of Climate System & Polar Meteorology, Chinese Academy of Meteorological Sciences, Beijing 100081, China
[4]College of Geography and Environment, Shandong Normal University, Jinan 250014, China
Correspondence to: Tong Zhang (tzhang@camscma.cn)

Abstract. By combining *in situ* measurements and a two-dimensional thermo-mechanically coupled ice flow model, we investigate the present thermal status of the largest valley glacier (Laohugou Glacier No.12; LHG12) in Mt. Qilian Shan located in the arid region of western China. Our model results suggest that LHG12, previously considered as fully cold, is probably polythermal, with a lower temperate ice layer overlain by an upper layer of cold ice over a large region of the ablation area. Modeled ice surface velocities match well with the *in situ* observations in the east branch (mainstream) but clearly underestimate the ice surface velocities near the glacier terminus possibly because the convergent flow is ignored and the basal sliding beneath the confluence area is underestimated. The modeled ice temperatures agree with the *in situ* measurements (with biases less than 0.5 K) from a deep borehole (110 m) in the upper ablation area. The model results are highly sensitive to surface thermal boundary conditions, for example, surface air temperature and near-surface ice temperature. In this study, we use a Dirichlet surface thermal condition constrained by 20 m borehole temperatures and annual surface air temperatures. Like many other alpine glaciers, strain heating is an important parameter controlling the englacial thermal structure in LHG12.

1 Introduction

The storage of water in glaciers is an important component of the hydrological cycle at different time scales (Jansson et al., 2003; Huss et al., 2010), especially in arid and semi-arid regions such as northwestern China, where many glaciers are currently retreating and disappearing (Yao et al., 2012; Neckel et al., 2014; Tian et al., 2014). Located on the northeastern edge of the Tibetan Plateau (36 – 39 °N, 94 – 104 °E), Mt. Qilian Shan (MQS) develops 2051 glaciers covering an area of approximately 1057 km^2 with a total ice volume of approximately 50.5 km^3 (Guo et al., 2014, 2015). Meltwater from MQS glaciers is a very important water resource for the agricultural irrigation and socio-economic development of the oasis cities in northwestern China. Thus, the changes in the MQS glaciers that occur as the climate becomes warmer in the near future are of concern.

Due to logistic difficulties, few MQS glaciers have been investigated in previous decades. However, Laohugou Glacier No.12 (hereafter referred to as LHG12), the largest valley glacier of MQS, has been investigated. Comprised of two branches (east and west), LHG12 is located on the north slope of western MQS (39°27' N, 96°32' E; Fig. 1), with a length of approximately 9.8 km, an area of approximately 20.4 km^2, and an elevation range of 4260 – 5481 m a.s.l. (Liu et al., 2011). LHG12 was first studied by a Chinese expedition from 1958 – 1962 and was considered again in short-term field campaigns in the 1970s and 1980s that were aimed at monitoring glacier changes (Du et al., 2008). Since 2008, the Chinese Academy of Sciences has operated a field station for obtaining meteorological and glaciological measurements of LHG12.

The temperature distribution of a glacier primarily controls the ice rheology, englacial hydrology, and basal sliding conditions (Blatter and Hutter, 1991; Irvine-Fynn et al., 2011; Schäfer et al., 2014). A good understanding of the glacier thermal conditions is importance for predicting glacier response to climate change (Wilson et al., 2013; Gilbert et al., 2015), improving glacier hazard analysis (Gilbert et al., 2014a), and reconstructing past climate histories (Vincent et al., 2007; Gilbert et al., 2010). The thermal regime of a glacier is mainly controlled by the surface thermal boundary conditions (e.g., Gilbert et al., 2014b; Meierbachtol et al., 2015). For example, near-surface warming from refreezing meltwater and cooling from the cold air of crevasses influence the thermal regimes of glaciers (Wilson and Flowers, 2013; Wilson et al., 2013; Gilbert et al., 2014a). Using both *in situ* measurements and numerical models, Meierbachtol et al. (2015) argued that shallow borehole ice temperatures served as better boundary constraints than surface air temperatures in Greenland. However, for the east Rongbuk glacier on Mt. Everest, which is considered polythermal, Zhang et al. (2013) found that the modeled ice temperatures agreed well with the *in situ* shallow borehole observations when using surface air temperatures as the surface thermal boundary condition. Therefore, careful investigation of the upper thermal boundary condition is highly necessary for glaciers in different regions under different climate conditions.

LHG12 is widely considered as an extremely continental type (cold) glacier and is characterized by low temperatures and precipitation (Huang, 1990; Shi and Liu, 2000). However, in recent years, we have observed extensive and widespread meltwater at the ice surfaces and glacier terminus. In addition, percolation of snow meltwater consistently occurs in the accumulation basin during the summer. Therefore, we address the following two pressing questions in this study: (i) What is the present thermal status of LHG12? and (ii) How do different surface thermal boundary conditions impact the modeled ice temperature and flow fields? Because warm ice can assist basal slip and accelerate glacier retreat, understanding the current thermal status of LHG12 is very important for predicting its future dynamic behaviour.

To answer these questions, we conduct diagnostic simulations for LHG12 by using a thermo-mechanically coupled first-order flow-band ice flow model. This paper is organized as follows: First, we provide a detailed description of the glaciological datasets of LHG12. Then, we briefly review the numerical ice flow model used in this study. After performing a set of model sensitivity experiments, we compare the model results with the measured ice surface velocities and the ice temperature profile obtained from a deep borehole. Next, we investigate the impacts of different surface thermal boundary conditions and assess the contributions of heat advection, strain heating, and basal sliding to the temperature field of LHG12. Finally, we discuss the limitations of our model and present the important conclusions that resulted from this study.

2 Field data

Most *in situ* observations, e.g., borehole ice temperatures, surface air temperatures and ice surface velocities, have been made on the east branch (mainstream) of LHG12 (Fig. 1). Measurements on the west branch are dispersed and temporally discontinuous. Thus, we only consider the *in situ* data from the east tributary when building our numerical ice flow model.

2.1 Glacier geometry

In July – August 2009 and 2014, two ground-penetrating radar (GPR) surveys were conducted on LHG12 using a pulseEKKO PRO system with center frequencies of 100 MHz (2009) and 50 MHz (2014) (Fig. 1b). Wang et al. (2016) have presented details regarding the GPR data collection and post-processing.

As shown in Fig. 2a, the east branch of LHG12 has a mean ice thickness of approximately 190 m. We observed the thickest ice layer (approximately 261 m) at 4864 m a.s.l. Generally, the ice surface of LHG12 is gently undulating, with a mean slope of 0.08°, and the bed of LHG12 shows significant overdeepening in the middle of the center flowline (CL) (Fig. 2a). To account for the lateral effects exerted by glacier valley walls in our 2D ice flow model, we parameterize the lateral drag using the glacier half widths. Based on the GPR measurements on LHG12, we parameterize the glacier cross-sections by a power law function $z = aW(z)^b$, where z and $W(z)$ are the vertical and horizontal distances from the lowest point of the profile, and a and b are constants representing the flatness and steepness of the glacier valley, respectively (Svensson, 1959). The b values for LHG12 range from 0.8 to 1.6, indicating that the valley containing LHG12 is approximately "V"-shaped (Wang et al., 2016). As an input for the flow-band ice flow model, the glacier width, W, was also calculated by ignoring all tributaries (including the west branch) (Fig. 1b and 2b).

2.2 Ice surface velocities

The surface velocities of the ice in LHG12 were determined from repeated surveys of stakes drilled into the ice surface. All stakes were located in the distance between km 0.6 – 7.9 along the CL (Fig. 3), spanning an elevation range of 4355 – 4990 m.a.s.l. (Fig. 1b). We measured the stake positions using a real-time kinematic (RTK) fixed solution by a South Lingrui S82 GPS system (Liu et al., 2011). The accuracy of the GPS positioning is an order of a few centimeters and the uncertainty of the calculated ice surface velocities is estimated to be less than 1 m a^{-1}. Because it is difficult to conduct fieldwork on LHG12 (due to, e.g., crevasses and supra-glacial streams), it was nearly impossible to measure all stakes each observational year. Thus, the current dataset includes annual ice surface velocities from 2008 – 2009 and 2009 – 2010, summer measurements from June 17 – August 30, 2008, and winter measurements from February 1 – May 28, 2010.

The *in situ* ice surface velocities shown in Fig. 3 are all from stakes near the CL (Fig. 1b). Small ice surface velocities ($<$ 17 m a^{-1}) are clearly visible in the upper accumulation (km 0 – 1.2) and lower ablation areas (km 6.5 – 9.0) (Fig. 3). Fast ice flow ($>$ 30 m a^{-1}) can be observed between elevations of 4700 – 4775 m a.s.l. (km 4.0 – 5.0), where the ice surface velocities during the summer are approximately 6 m a^{-1} greater than the annual mean velocity ($<$ 40 m a^{-1}). Measurements of winter

ice surface velocities (< 10 m a^{-1}) are only available near the glacier terminus showing a clear inter-annual variation of the ice flow speeds.

2.3 Surface air temperature

Two automatic weather stations (AWS) were deployed on LHG12, one in the ablation area at 4550 m a.s.l. (site 1, Fig. 1b), and one in the accumulation area at 5040 m a.s.l. (site 3). During the period of 2010 – 2013, the mean annual air temperatures (2 m above the ice surface) at sites 1 and 3 were $-9.2\,^{\circ}$C and $-12.2\,^{\circ}$C, respectively, suggesting a lapse rate of -0.0061 K m^{-1}. These results were used to calculate the distribution of the surface air temperatures at all elevations on LHG12.

2.4 Borehole ice temperature

In August 2009 and 2010, we drilled three 25 m deep shallow boreholes on LHG12 (Fig. 1b). One borehole was drilled in the upper ablation area (site 2, approximately 4900 m a.s.l.) and two boreholes were drilled at the AWS locations (sites 1 and 3). The snow/ice temperatures were measured at the boreholes during the period of October 1, 2010 – September 30, 2011. The seasonal variations of the snow/ice temperatures in the shallow boreholes are presented in Figs. 4a, b and c. Our measurements show very little fluctuation (±0.4 K) in the ice temperatures over the depth range of 20 – 25 m. Below the 3 m depth, the annual mean temperature profiles for sites 1 and 2 show a linearly increase in temperature with depth, while the annual mean temperature profile for site 3 is convex upward. The mean annual 20 m ice temperatures (T_{20m}) at sites 1, 2, and 3 are 5.5 K, 3.0 K, and 9.5 K higher than the mean annual air temperatures (T_{air}), respectively. Despite its higher elevation, the near-surface snow/ice temperatures below a depth of 5 m at site 3 are greater than the near-surface snow/ice temperatures in the ablation area (sites 1 and 2), largely due to the latent heat released as the meltwater entrapped in the surface snow layers refreezes, as observed in many previous field expeditions.

To determine the englacial thermal conditions of LHG12, we drilled a deep ice core (167 m) in the upper ablation area of LHG12 (approximately 4971 m a.s.l., Fig. 1b). In October 2011, ice temperature were measured to a depth of approximately 110 m using a thermistor string after 20 days of the drilling, as shown in Fig. 4d. The string consists of 50 temperature sensors with a vertical spacing of 0.5 m and 10 m at the ice depths of 0 – 20 m and 20 – 110 m, respectively. The accuracy of the temperature sensor is around ±0.05 K (Liu et al., 2009). From Fig. 4d we can see that the temperature profile is close to linear with a temperature gradient of around 0.1 K m^{-1} at the depths of 9 – 30 m. Below the depth of 30 m, the ice temperature also demonstrates a linear relationship with depth but with a smaller temperature gradient of around 0.034 K m^{-1}.

3 Model description

In this study, we used the same two-dimensional (2D), thermo-mechanically coupled, first-order, flow-band ice flow model as Zhang et al. (2013). Therefore, we only address a very brief review of the model here.

3.1 Ice flow model

We define x, y, and z as the horizontal along-flow, horizontal across-flow and vertical coordinates, respectively. By assuming the vertical normal stress as hydrostatic and neglecting the bridging effects (Pattyn, 2002), the equation for momentum balance is given as

$$\frac{\partial}{\partial x}(2\sigma'_{xx} + \sigma'_{yy}) + \frac{\partial \sigma'_{xy}}{\partial y} + \frac{\partial \sigma'_{xz}}{\partial z} = \rho g \frac{\partial s}{\partial x}, \tag{1}$$

where σ'_{ij} is the deviatoric stress tensor, ρ is the ice density, g is the gravitational acceleration, and s is the ice surface elevation. The parameters used in this study are given in Table 1.

The constitutive relationship of ice dynamics is described by the Glen's flow law (Cuffey and Paterson, 2010)

$$\sigma'_{ij} = 2\eta \dot{\epsilon}_{ij}, \quad \eta = \frac{1}{2}A^{-1/n}(\dot{\epsilon}_e + \dot{\epsilon}_0)^{(1-n)/n}, \tag{2}$$

where η is the ice viscosity, $\dot{\epsilon}_{ij}$ is the strain rate, n is the flow law exponent, A is the flow rate factor, $\dot{\epsilon}_e$ is the effective strain rate, and $\dot{\epsilon}_0$ is a small number used to avoid singularity. The flow rate factor is parameterized using the Arrhenius relationship as

$$A(T) = A_0 \exp(-\frac{Q}{RT}), \tag{3}$$

where A_0 is the pre-exponential constant, Q is the activation energy for creep, R is the universal gas constant, and T is the ice temperature. The effective strain rate $\dot{\epsilon}_e$ is related to the velocity gradient by

$$\dot{\epsilon}_e^2 \simeq \left(\frac{\partial u}{\partial x}\right)^2 + \left(\frac{\partial v}{\partial y}\right)^2 + \frac{\partial u}{\partial x}\frac{\partial v}{\partial y} + \frac{1}{4}\left(\frac{\partial u}{\partial y}\right)^2 + \frac{1}{4}\left(\frac{\partial u}{\partial z}\right)^2, \tag{4}$$

where u and v are the velocity components along the x and y direction, respectively. By assuming $\partial v/\partial y = (u/W)(\partial W/\partial x)$, we parameterize the lateral drag, σ'_{xy}, as a function of the flow-band half width, W, following Flowers et al. (2011)

$$\sigma'_{xy} = -\frac{\eta u}{W}. \tag{5}$$

For an easy numerical implementation, we reformulate the momentum balance equation (1) as

$$\frac{u}{W}\left\{2\frac{\partial \eta}{\partial x}\frac{\partial W}{\partial x} + 2\eta\left[\frac{\partial^2 W}{\partial x^2} - \frac{1}{W}\left(\frac{\partial W}{\partial x}\right)^2\right] - \frac{\eta}{W}\right\}$$
$$+ \frac{\partial u}{\partial x}\left(4\frac{\partial \eta}{\partial x} + \frac{2\eta}{W}\frac{\partial W}{\partial x}\right) + \frac{\partial u}{\partial z}\frac{\partial \eta}{\partial z} + 4\eta\frac{\partial^2 u}{\partial x^2} + \eta\frac{\partial^2 u}{\partial z^2} = \rho g\frac{\partial s}{\partial x}, \tag{6}$$

where the ice viscosity is defined as

$$\eta = \frac{1}{2}A^{-1/n}\left[\left(\frac{\partial u}{\partial x}\right)^2 + \left(\frac{u}{W}\frac{\partial W}{\partial x}\right)^2 + \frac{u}{W}\frac{\partial u}{\partial x}\frac{\partial W}{\partial x} + \frac{1}{4}\left(\frac{\partial u}{\partial z}\right)^2 + \frac{1}{4}\left(\frac{u}{W}\right)^2 + \dot{\epsilon}_0^2\right]^{(1-n)/2n}. \tag{7}$$

3.2 Ice temperature model

The ice temperature field can be calculated using a 2D heat transfer equation (Pattyn, 2002),

$$k\left(\frac{\partial^2 T}{\partial x^2} + \frac{\partial^2 T}{\partial z^2}\right) - \rho c_p\left(u\frac{\partial T}{\partial x} + w\frac{\partial T}{\partial z}\right) + 4\eta\dot{\epsilon}_e^2 = 0, \tag{8}$$

where w is the vertical ice velocity, k and c_p are the thermal conductivity and heat capacity of the ice, respectively.

5   The pressure melting point of the ice, T_{pmp}, is described by the Clausius-Clapeyron relationship

$$T_{\text{pmp}} = T_0 - \beta(s - z), \tag{9}$$

where T_0 is the triple-point temperature of water and β is the Clausius-Clapeyron constant. Following Zhang et al. (2013), we determined the position of the cold-temperate ice transition surface (CTS) by considering the following two cases: (i) melting condition, i.e., cold ice flows downward into the temperate ice zone, and (ii) freezing condition, i.e., temperate ice flows upward

10   into the cold ice zone (Blatter and Hutter, 1991; Blatter and Greve, 2015). For the melting case, the ice temperature profile at the CTS simply follows a Clausius-Clapeyron gradient (β). However, for the freezing case, the latent heat, Q_r, that is released when the water contained in the temperate refreezes is determined as (Funk et al., 1994)

$$Q_r = w\omega\rho_w L, \tag{10}$$

where ω is the fractional water content of the temperate ice, ρ_w is the water density and L is the latent heat of freezing. In this

15   case, following (Funk et al., 1994), the ice temperature gradient at the CTS can be described as

$$\frac{\partial T}{\partial z} = -\frac{Q_r}{k} + \beta. \tag{11}$$

3.3 Boundary conditions

In the ice flow model, we assume a stress-free condition for the glacier surface, and use the Coulomb friction law to describe the ice-bedrock interface where the ice slips (Schoof, 2005),

20    $$\tau_b = \Gamma\left(\frac{u_b}{u_b + \Gamma^n N^n \Lambda}\right)^{1/n} N, \qquad \Lambda = \frac{\lambda_{\max} A}{m_{\max}}, \tag{12}$$

where τ_b and u_b are the basal drag and velocity, respectively, N is the basal effective pressure, $\lambda_{\max}$ is the dominant wavelength of the bed bumps, $m_{\max}$ is the maximum slope of the bed bumps, and Γ and Λ are geometrical parameters (Gagliardini et al., 2007). Here we take $\Gamma = 0.84 m_{\max}$ following Flowers et al. (2011) and Zhang et al. (2013). The basal effective pressure in the friction law, N, is defined as the difference between the ice overburden pressure and the basal water pressure (Gagliardini

25   et al., 2007; Flowers et al., 2011),

$$N = \rho g H - P_w = \phi\rho g H, \tag{13}$$

where H and P_w are the ice thickness and basal water pressure, respectively, and ϕ implies the ratio of basal effective pressure to the ice overburden pressure. The basal drag is defined as the sum of all resistive forces (Van der Veen, 1989; Pattyn, 2002). It should be noted that the basal sliding is only permitted when basal ice temperature reaches the local pressure-melting point.

We apply a Dirichlet temperature constraint (T_{sbc}) on the ice surface in the temperature model. In some studies, $T_{sbc} = T_{air}$ is used (e.g. Zhang et al., 2013), which, as suggested by recent studies, could result in lower velocity values (Sugiyama et al., 2014) and cold bias in ice temperature simulations (Meierbachtol et al., 2015). By contrast, Meierbachtol et al. (2015) recommended using the snow/ice temperature at the depth where inter-annual variations of air temperatures are damped (15 – 20 m, T_{dep}) (a proxy for the annual mean ice surface temperature). One advantage of using T_{dep} is that the effects of refreezing meltwater and the thermal insulation of winter snow can be included in the model (Huang et al., 1982; Cuffey and Paterson, 2010). In fact, the condition $T_{dep} = T_{air}$ is acceptable only in dry and cold snow zones (Cuffey and Paterson, 2010); however, $T_{dep} > T_{air}$ is often observed in zones where meltwater is refreezing in glaciers, such as the LHG12 (Fig. 4). In this study, we set T_{sbc} in the accumulation zone to the 20 m borehole temperature measured at site 3, while T_{sbc} in the ablation area is prescribed by a simple parameterization (Lüthi and Funk, 2001; Gilbert et al., 2010)

$$T_{sbc} = \begin{cases} T_{20m}, & \text{in the accumulation zone,} \\ T_{air} + c, & \text{in the ablation zone,} \end{cases} \tag{14}$$

where c is a tuning parameter including the impacts of both the surface energy budget and the steady-state temperature (Gilbert et al., 2010). We denote Eq. (14) as the surface thermal boundary condition of the reference experiment (E-ref) after comparing the other two numerical experiments by setting $T_{sbc} = T_{air}$ (E-air) and $T_{sbc} = T_{20m}$ (E-20m) (see Sect. 4.3 for details).

At the ice-bedrock interface, we apply the following Neumann-type boundary condition in the temperature model,

$$\frac{\partial T}{\partial z} = -\frac{G}{k}, \tag{15}$$

where G is the geothermal heat flux. We here use a constant geothermal heat flux, 40 mW m^{-2}, an *in situ* measurement from the Dunde ice cap in the western MQS (Huang, 1999), over the entire model domain.

3.4 Numerical solution

In our model we use a finite difference discretization method and a terrain-following coordinate transformation. The numerical mesh we use contains 61 grids in x and 41 layers in z. The ice flow model (Eq. (6)) is discretized with a second-order centered difference scheme while the ice temperature model (Eq. (8)) employs a first-order upstream difference scheme for the horizontal heat advection term and a node-centered difference scheme for the vertical heat advection term and the heat diffusion terms. The velocity and temperature fields are iteratively solved by a relaxed Picard subspace iteration scheme (De Smedt et al., 2010) in Matlab.

4 Model results and discussions

To understand the present thermal status of LHG12, we assume a thermal steady-state condition and perform a series of thermo-mechanically coupled diagnostic simulations using a 2D first-order flow-band model (described in above). First, we simulate the ice velocity and temperature fields for LHG12 by investigating the sensitivities of the model to geometrical bed parameters

(λ_{max} and m_{max}), ratio of basal effective pressure (ϕ), water content (ω), geothermal heat flux (G), valley shape index (b), and surface thermal boundary parameter c. We then inspect three different surface thermal boundary conditions (E-ref, E-air, and E-20m) by comparing their model outputs with *in situ* ice temperature observations in the deep borehole at site 3. In addition, we perform four experiments (E-advZ, E-advX, E-strain, and E-slip) to investigate the impacts of heat advection, strain heating, and basal sliding on the thermal field and flow characteristics of LHG12.

4.1 Parameter sensitivity

As shown in Figs. 5 and 6, we conduct a series of sensitivity experiments to investigate the relative importance of different model parameters (λ_{max}, m_{max}, ϕ, ω, G, b, c) on ice flow speeds and temperate ice zone (TIZ) sizes by varying the value of one parameter while holding the other parameters fixed.

The friction law parameters, λ_{max} and m_{max}, which describe the geometries of bedrock obstacles (Gagliardini et al., 2007; Flowers et al., 2011), have non-negligible impacts on the model results. As shown in Figs. 5a and b, the modeled velocities and TIZ sizes increase as λ_{max} increases and m_{max} decreases, similar to in the results observed by Flowers et al. (2011) and Zhang et al. (2013). A large increase in the modeled velocity occurs when $m_{max} < 0.2$. The ratio, ϕ, is an insensitive parameter in our model when it is larger than 0.3 (Fig. 5c). Although the water content, ω, in the ice does not directly impact the ice velocity simulations (the flow rate factor A is assumed independent of the water content in ice), the water content can affect the temperature field and, consequently, influence A and the ice velocities (Fig. 5d). From Fig. 6d, we can clearly see that increasing the water content may result in larger TIZ sizes. For example, changing the water content from 1% to 3% nearly doubles the TIZ thickness over a horizontal distance of km $3.5 - 5.8$. In addition, we test the sensitivity of the model to different geothermal heat flux values. A larger geothermal heat flux can result in larger TIZs but has a limited impact on modeling ice velocity (Figs. 5e and 6e). As shown by Zhang et al. (2013), our model results are mainly controlled by the shape of the glacial valley, specifically the b index (Sect. 2.1). A large value of b indicates a flat glacial valley and suggests that a small lateral drag was exerted on the ice flow (Figs. 5f and 6f).

Further, we vary the values of c from 0 to 6 K (with a step size of 0.2 K) and compare the modeled 20 m borehole temperatures with *in situ* annual measurements at sites 1 and 2 (Fig. 7). As shown in Fig. 1b, site 1 is located at the center of the confluence area where the convergent flow from the west branch joins the mainstream. Thus, at site 1 it is difficult to find a good c value that predicts close temperature match to the observations (Fig. 7a). We therefore determine the c value (1.6 K) based on the fittings between the modeled and observed ice temperature data at site 2.

Based on the sensitivity experiments described above, we adopt a parameter set of $\lambda_{max} = 4$ m, $m_{max} = 0.3$, $\phi = 1$ (no basal water pressure), $\omega = 3\%$, $G = 40$ mW m^{-2}, $b = 1.2$, and $c = 1.6$ K as a diagnostic reference in our modeling experiment (E-ref).

4.2 Comparison with *in situ* observations

In the reference experiment (E-ref), we simulate the distributions of horizontal ice velocities and temperatures (Figs. 8a and c). Next, the model results are compared to the measured ice surface velocities and the ice temperature profile in the deep

borehole (Figs. 8b and d). Generally, the modeled ice surface velocities agree well with *in situ* observations from the glacier head to km 4.8 along the CL (Fig. 8b). However, from 4.8 km to the glacier terminus, our model generally underestimates the ice surface velocities as shown in all simulations in Fig. 5, which may possibly result from the neglect of the convergent flow from the west branch and an enhanced basal sliding which is not captured by our model in the confluence area. We verify this

5 hypothesis by conducting two other experiments, E-W and E-WS. In E-W the glacier widths are increased by 450 m at km 5.8 – 7.3 as a proxy of including the impact of the convergent flow from the west branch (Fig. 9). In E-WS, except for the same glacier width increase as in E-W, we also increase λ_{max} by 200% and decrease m_{max} by 60% for accelerating the basal sliding at km 5.8 – 7.3 (Fig. 9). We can clearly find that while both factors have a non-negligible contribution to the model results, the basal sliding may play a bit more important role in the confluence area. This indicates a need of considering glacier flow

10 branches and spatially variable sliding law parameters in real glacier modeling studies.

The model predicts a TIZ overlain by cold ice over a horizontal distance of km 1.1 – 6.4 (Fig. 8c). In addition, we further validated our numerical model by using *in situ* 110 m deep ice temperature measurements (Fig. 8d). In this study, we use a 2D model approach that neglects ice fluxes and heat fluxes along the y direction. Consequently, it is very difficult to obtain numerical temperature results that agree perfectly with the *in situ* observations. However, as shown in Fig. 8d, a match can be

15 found between the model results and *in situ* measurements at depths of approximately 20 – 40 m and 80 – 90 m. The model overestimates the ice temperatures at depths of approximately 50 – 70 m and underestimates the ice temperatures at depths of approximately 100 – 110 m (by less than 0.5 K). Because *in situ* ice temperature data from below 110 m have not been obtained, we were unable to compare the modeled and measured ice temperatures at the ice-bedrock interface.

4.3 Choice of surface thermal boundary condition

20 We conduct three different numerical experiments (E-air, E-20m, and E-ref) to investigate the impacts of different surface thermal boundary conditions on the thermo-mechanical fields of LHG12. For the E-air and E-20m experiments, we set $T_{sbc} = T_{air}$ and $T_{sbc} = T_{20m}$, respectively. E-ref is adopted in our "real" LHG12 simulations, which uses the $T_{sbc} = T_{20m}$ in the accumulation basin and the $T_{sbc} = T_{air} + c$ ($c = 1.6$ K) in the ablation area.

The intercomparison results of E-air, E-20m, and E-ref for ice velocities and temperatures are presented in Fig. 10. The ice

25 temperatures along the CL are highly sensitive to T_{sbc}. From E-air, it is observed that LHG12 becomes fully cold, with an average field temperature 5.3 K colder than that of E-ref (Fig. 10a), which decreases the ice surface velocity by approximately 10.0 m a^{-1} (Fig. 10b). Compared with E-ref, E-20m results in larger T_{sbc} values in the ablation area, greater mean ice temperatures (by approximately 1.5 K; Fig. 10a), greater TIZ thicknesses (by approximately 9.7 m over a region of km 2.1 – 5.9; Fig. 10c), and faster ice surface velocities (by approximately 1.5 m a^{-1}; Fig. 10b). Next, we compare the ice temperature modeling

30 results with the *in situ* observations of the deep borehole at site 3 (Fig. 10d). E-ref results in the best simulation results, and E-20m, though generally similar to E-ref, generates warmer ice above a depth of 80 m in the deep borehole. Unsurprisingly, E-air results in an unreliable temperature profile that is colder than the actual temperatures at all depths.

As noted above, the dynamics of LHG12 can be strongly influenced by the choices of different surface thermal boundary conditions. For LHG12, most accumulation and ablation events overlap during the summer season (Sun et al., 2012). The

meltwater entrapped in snow and moulins during the summer season can release large amounts of heat due to refreezing when the temperature decreases, which may significantly increase the ice temperatures in the near-surface snow/ice layers (Fig. 4) and result in the warm bias of T_{20m} (compared with the mean annual surface air temperature). Therefore, compared with E-air, the E-ref and E-20m experiments better incorporate the effects of meltwater refreezing in the accumulation basin into the
5 prescribed surface thermal boundary constraints resulting in more accurate simulations of ice temperature and flow fields.

4.4 Roles of heat advection, strain heating and basal sliding

To assess the relative contributions of heat advection and strain heating to the thermo-mechanical field of LHG12, we conducted three experiments (E-advZ, E-advX, and E-strain), in which the vertical advection, horizontal along-flow advection and strain heating were neglected, respectively. In addition, to investigate the effects of basal sliding predicted by the Coulomb friction
10 law on the thermal state and flow dynamics of LHG12, we performed an experiment (E-slip) with $u_b = 0$.

Figs. 11 and 12 compare the ice velocity and temperature results of E-advZ, E-advX, E-strain and E-slip with those of E-ref. If the vertical advection is neglected (E-advZ; cold ice at the glacier surface cannot be transported downwards into the interior of LHG12), LHG12 becomes warmer (Figs. 11a and c) and flows faster relative to other experiments (Fig. 11b). As described for the discontinuous surface thermal boundary conditions across the ELA (a straightforward result from the refreezing meltwater
15 in the accumulation basin), a discontinuous transition of the mean column ice temperature was observed along the CL at km 1.3 (the horizontal position of ELA) in E-advX (Fig. 11a). Compared with E-ref, the E-advX experiment predicted colder field temperatures (by approximately 2.7 K) and much smaller surface ice velocities (< 15.4 m a^{-1}). Because the accumulation basin of LHG12 is relatively warm, E-advX, which neglects the horizontal transport of ice from upstream and downstream, predicts much colder conditions for LHG12, i.e., the modeled temperate ice only appears at three discontinuous grid points
20 (Fig. 11c). As described by Zhang et al. (2015), we observed that strain heating contributes greatly to the thermal configuration of LHG12. If we leave away the strain heating (E-strain), LHG12 becomes fully cold, with a mean ice temperature field lower than that of E-ref by approximately 0.9 K. Consequently, the E-strain experiment predicts lower ice surface velocities (Fig. 12b). Previous studies have suggested that basal sliding can significantly influence the thermal structures and velocity fields of glaciers (e.g. Wilson et al., 2013; Zhang et al., 2015). However, in this study the neglect of basal sliding (E-slip) results
25 in a temperature field very similar to that of E-ref. We attribute this difference to the relatively small modeled basal sliding values for LHG12. The observed and modeled ice temperature profiles of E-advZ, E-advX, E-strain, E-slip, and E-ref are also compared for the deep ice borehole in Figs. 11d and 12d. The differences of the profiles can also be explained by our above explanations.

4.5 Model limitations

30 Although our 2D, first-order, flow-band model can account for part of the three-dimensional nature of LHG12 by parameterizing the lateral drag with glacier width variations, it cannot fully describe the ice flow along the y direction, and are not able to account for the confluence of glacier tributaries. The shape of the LHG12 glacier valley is described using a constant value for index b (1.2; approximately "V" type cross-sections), which was determined from several traverse GPR profiles (Fig. 1).

However, for real glaciers, the cross-sectional geometry profiles are generally complex, resulting in an inevitable bias when we idealize the glacier cross-sectional profiles by using power law functions across the entire LHG12 area. Although the regularized Coulomb friction law provides a physical relationship between the basal drag and sliding velocities, several parameters (e.g., $\lambda_{\max}$, $m_{\max}$) still must be prescribed based on surface velocity observations. Another uncertainty could be from the spatially uniform geothermal heat flux that we assume in the model, as it may have a great spatial variation due to the mountain topography (Lüthi and Funk, 2001). In addition, we can also improve our model ability by linking the water content in the temperate ice layer to a physical thermo-hydrological process in the future.

Due to the limitations of *in situ* shallow borehole ice temperature measurements, the surface thermal boundary condition in our temperature model is determined using a simple parameterization based on observations at three elevations (Fig. 1b). In addition, the parameterized surface thermal boundary condition only provides a rough estimate of the overall contributions of the heat from refreezing meltwater and ice flow advection. At this stage, we cannot simulate the actual physical process involved in the transport of near-surface heat from refreezing, which has been suggested by (Gilbert et al., 2012; Wilson and Flowers, 2013). The assumption of steady state neglects the transient effects of past climate and glacier changes, which can have a very important impact on the shape of temperature profile (Lüthi et al., 2015; Gilbert et al., 2015).

5 Conclusions

For the first time, we investigate the thermo-mechanical features of a typical valley glacier, Laohugou Glacier No.12 (LHG12), in Mt. Qilian Shan, which is an important fresh water source for the arid regions in western China. We assess the present thermal status of LHG12 using a two-dimensional thermo-mechanically coupled first-order flow-band model using available *in situ* measurements of glacier geometries, borehole ice temperatures, and surface meteorological and velocity observations. By carefully comparing modeled ice velocities and temperatures with *in situ* observations, we conduct a set of numerical sensitivity experiments that include, for example, basal sliding parameters, geothermal heat fluxes and glacial valley shapes. In addition, we investigate the impacts of different surface thermal conditions (surface air and near-surface ice temperatures), heat advection, strain heating, and basal sliding on our numerical model results.

Similar to other alpine land-terminating glaciers, the mean annual horizontal ice flow speeds of LHG12 are relatively low (less than 40 m a^{-1}). However, we observed large inter-annual variations in the ice surface velocity during the summer and winter seasons. Due to the release of heat from refreezing meltwater, the observed ice temperatures for the shallow ice borehole in the accumulation basin (site 3; Fig. 1) are higher than for the temperatures at sites 1 and 2 at lower elevations, indicating the existence of meltwater refreezing, as observed in our field expeditions. Thus, we parameterize the surface thermal boundary condition by accounting for the 20 m deep temperature instead of only the surface air temperatures. We observed that LHG12 has a polythermal structure with a temperate ice zone that is overlain by cold ice near the glacier base throughout a large region of the ablation area.

Horizontal heat advection is important on LHG12 for bringing the relatively warm ice in the accumulation basin (due to the heat from refreezing meltwater) to the downstream ablation zone. In addition, vertical heat advection is important for trans-

porting the near-surface cold ice downwards into the glacier interior, which "cools down" the ice temperature. Furthermore, we argue that the strain heating of LHG12 also plays an important role in controlling the englacial thermal status, as suggested by Zhang et al. (2015). However, we also observed that simulated basal sliding contributes little to the thermal-mechanical configuration of LHG12 (very small; < 4 m a^{-1}).

5   The mean annual surface air temperature could serve as a good approximation for the temperatures of shallow ice, where seasonal climate variations are damped at cold and dry locations (Cuffey and Paterson, 2010). However, for LHG12, using the mean annual surface air temperature as the thermal boundary condition at the ice surface would predict an entirely cold glacier with very small ice flow speeds. Because warming is occurring on alpine glaciers in, for example, Mt. Himalayas and Qilian Shan, further studies of supra-glacial and near-surface heat transport are very important because they will affect the surface

10 thermal conditions and, eventually, the dynamical behaviours of the glacier.

References

Blatter, H. and Greve, R.: Comparison and verification of enthalpy schemes for polythermal glaciers and ice sheets with a one-dimensional model, Polar Science, 9, 196–207, 2015.

Blatter, H. and Hutter, K.: Polythermal conditions in Arctic glaciers, Journal of Glaciology, 37, 261–269, 1991.

5   Cuffey, K. and Paterson, W.: The Physics of Glaciers, Elsevier, Amsterdam, 4th edn., 2010.

De Smedt, B., Pattyn, F., and De Groen, P.: Using the unstable manifold correction in a Picard iteration to solve the velocity field in higher-order ice-flow models, Journal of Glaciology, 56, 257–261, 2010.

Du, W., Qin, X., Liu, Y., and Wang, X.: Variation of the Laohugou Glacier No.12 in the Qilian Mountains. (in Chinese with English summary), Journal of Glaciology and Geocryology, 30, 373–379, 2008.

10   Flowers, G. E., Roux, N., Pimentel, S., and Schoof, C. G.: Present dynamics and future prognosis of a slowly surging glacier, The Cryosphere, 5, 299–313, 2011.

Funk, M., Echelmeyer, K. A., and Iken, A.: Mechanisms of fast flow in Jakobshavn Isbræ, West Greenland: Part II. Modeling of englacial temperatures, Journal of Glaciology, 40, 569–585, 1994.

Gagliardini, O., Cohen, D., Råback, P., and Zwinger, T.: Finite-element modeling of subglacial cavities and related friction law, Journal of
15   Geophysical Research, 112, F02 027, 2007.

Gilbert, A., Wagnon, P., Vincent, C., Ginot, P., and Funk, M.: Atmospheric warming at a high-elevation tropical site revealed by englacial temperatures at Illimani, Bolivia (6340 m above sea level, 16°S, 67°W), Journal of Geophysical Research, 115, D10 109, 2010.

Gilbert, A., Vincent, C., Wagnon, P., Thibert, E., and Rabatel, A.: The influence of snow cover thickness on the thermal regime of Tête Rousse Glacier (Mont Blanc range, 3200 m a.s.l.): Consequences for outburst flood hazards and glacier response to climate change, Journal of
20   Geophysical Research, 117, 2012.

Gilbert, A., Gagliardini, O., Vincent, C., and Wagnon, P.: A 3-D thermal regime model suitable for cold accumulation zones of polythermal mountain glaciers, Journal of Geophysical Research: Earth Surface, 119, 1876–1893, 2014a.

Gilbert, A., Vincent, C., Six, D., Wagnon, P., Piard, L., and Ginot, P.: Modeling near-surface firn temperature in a cold accumulation zone (Col du Dôme, French Alps): from a physical to a semi-parameterized approach, The Cryosphere, 8, 689–703, 2014b.

25   Gilbert, A., Vincent, C., Gagliardini, O., Krug, J., and Berthier, E.: Assessment of thermal change in cold avalanching glaciers in relation to climate warming, Geophysical Research Letters, 42, 6382–6390, 2015.

Guo, W., Xu, J., Liu, S., Shangguan, D., Wu, L., Yao, X., Zhao, J., Liu, Q., Jiang, Z., Li, P., Wei, J., Bao, W., Yu, P., Ding, L., Li, G., Ge, C., and Wang, Y.: The second glacier inventory dataset of China (Version 1.0), Cold and Arid Regions Science Data Center at Lanzhou, 2014.

30   Guo, W., Liu, S., Xu, J., Wu, L., Shangguan, D., Yao, X., Wei, J., Bao, W., Yu, P., Liu, Q., and Jiang, Z.: The second Chinese glacier inventory: data, methods and results, Journal of Glaciology, 61, 357–372, 2015.

Huang, M.: On the temperature distribution of glaciers in China, Journal of Glaciology, 36, 210–216, 1990.

Huang, M.: Forty year's study of glacier temperature in China. (in Chinese with English summary), Journal of Glaciology and Geocryology, 21, 193–199, 1999.

35   Huang, M., Wang, Z., and Ren, J.: On the temperature regime of continental-type glaciers in China, Journal of Glaciology, 28, 117–128, 1982.

Huss, M., Jouvet, G., Farinotti, D., and Bauder, A.: Future high-mountain hydrology: a new parameterization of glacier retreat, Hydrology and Earth System Sciences, 14, 815–829, 2010.

Irvine-Fynn, T. D. L., Hodson, A. J., Moorman, B. J., Vatne, G., and Hubbard, A. L.: Polythermal glacier hydrology: A review, Reviews of Geophysics, 49, 2011.

5   Jansson, P., Hock, R., and Schneider, T.: The concept of glacier storage: a review, Journal of Hydrology, 282, 116–129, 2003.

Liu, Y., Hou, S., Wang, Y., and Song, L.: Distribution of borehole temperature at four high-altitude alpine glaciers in Central Asia, Journal of Mountain Science, 6, 221–227, 2009.

Liu, Y., Qin, X., Du, W., Sun, W., and Hou, D.: The movement features analysis of Laohugou Glacier No.12 in Qilian Mountains, Sciences in Cold and Arid Regions, 3, 119–123, 2011.

10 Lüthi, M. P. and Funk, M.: Modelling heat flow in a cold, high-altitude glacier: interpretation of measurements from Colle Gnifetti, Swiss Alps, Journal of Glaciology, 47, 314–324, 2001.

Lüthi, M. P., Ryser, C., Andrews, L. C., Catania, G. A., Funk, M., Hawley, R. L., Hoffman, M. J., and Neumann, T. A.: Heat sources within the Greenland Ice Sheet: dissipation, temperate paleo-firn and cryo-hydrologic warming, The Cryosphere, 9, 245–253, 2015.

Meierbachtol, T. W., Harper, J. T., Johnson, J. V., Humphrey, N. F., and Brinkerhoff, D. J.: Thermal boundary conditions on western Green-

15 land: Observational constraints and impacts on the modeled thermomechanical state, Journal of Geophysical Research: Earth Surface, 120, 623–636, 2015.

Neckel, N., Kropáček, J., Bolch, T., and Hochschild, V.: Glacier mass changes on the Tibetan Plateau 2003–2009 derived from ICESat laser altimetry measurements, Environmental research letters, 9, 014 009, 2014.

Pattyn, F.: Transient glacier response with a higher-order numerical ice-flow model, Journal of Glaciology, 48, 467–477, 2002.

20 Schäfer, M., Gillet-Chaulet, F., Gladstone, R., Pettersson, R., A. Pohjola, V., Strozzi, T., and Zwinger, T.: Assessment of heat sources on the control of fast flow of Vestfonna ice cap, Svalbard, The Cryosphere, 8, 1951–1973, 2014.

Schoof, C.: The effect of cavitation on glacier sliding, Royal Society of London Proceedings Series A, 461, 609–627, 2005.

Shi, Y. and Liu, S.: Estimation on the response of glaciers in China to the global warming in the 21st century, Chinese Science Bulletin, 45, 668–672, 2000.

25 Sugiyama, S., Sakakibara, D., Matsuno, S., Yamaguchi, S., Matoba, S., and Aoki, T.: Initial field observations on Qaanaaq ice cap, north-western Greenland, Annals of Glaciology, 55, 25–33, 2014.

Sun, W., Qin, X., Ren, J., Yang, X., Zhang, T., Liu, Y., Cui, X., and Du, W.: The surface energy budget in the accumulation zone of the Laohugou Glacier No.12 in the western Qilian Mountains, China, in summer 2009, Arctic, Antarctic, and Alpine Research, 44, 296–305, 2012.

30 Svensson, H.: Is the cross-section of a glacial valley a parabola?, Journal of Glaciology, 3, 362–363, 1959.

Tian, H., Yang, T., and Liu, Q.: Climate change and glacier area shrinkage in the Qilian Mountains, China, from 1956 to 2010, Annals of Glaciology, 55, 187–197, 2014.

Van der Veen, C. J.: A numerical scheme for calculating stresses and strain rates in glaciers, Mathematical geology, 21, 363–377, 1989.

Vincent, C., Le Meur, E., Six, D., Possenti, P., Lefebvre, E., and Funk, M.: Climate warming revealed by englacial temperatures at Col du

35 Dôme (4250 m, Mont Blanc area), Geophysical Research Letters, 34, L16 502, 2007.

Wang, Y., Ren, J., Qin, X., Liu, Y., Zhang, T., Chen, J., Li, Y., and Qin, D.: Ice depth and glacier-bed characteristics of Laohugou Glacier No.12, Qilian Mountains, revealed by ground-penetrating radar. (in Chinese with English summary), Journal of Glaciology and Geocry-ology, 1, 28–35, 2016.

Wilson, N. J. and Flowers, G. E.: Environmental controls on the thermal structure of alpine glaciers, The Cryosphere, 7, 167–182, 2013.

Wilson, N. J., Flowers, G. E., and Mingo, L.: Comparison of thermal structure and evolution between neighboring subarctic glaciers, Journal of Geophysical Research: Earth Surface, 118, 1443–1459, 2013.

Yao, T., Thompson, L., Yang, W., Yu, W., Gao, Y., Guo, X., Yang, X., Duan, K., Zhao, H., and Xu, B.: Different glacier status with atmospheric circulations in Tibetan Plateau and surroundings, Nature Climate Change, 2, 663–667, 2012.

Zhang, T., Xiao, C., Colgan, W., Qin, X., Du, W., Sun, W., Liu, Y., and Ding, M.: Observed and modelled ice temperature and velocity along the main flowline of East Rongbuk Glacier, Qomolangma (Mount Everest), Himalaya, Journal of Glaciology, 59, 438–448, 2013.

Zhang, T., Ju, L., Leng, W., Price, S., and Gunzburger, M.: Thermomechanically coupled modelling for land-terminating glaciers: a comparison of two-dimensional, first-order and three-dimensional, full-Stokes approaches, Journal of Glaciology, 61, 702–712, 2015.

Table 1. Parameters used in this study

| Symbol	Description	Value	Unit
β	Clausius-Clapeyron constant	8.7×10^{-4}	$K\,m^{-1}$
g	Gravitational acceleration	9.81	$m\,s^{-2}$
ρ	Ice density	910	$kg\,m^{-3}$
ρ_w	Water density	1000	$kg\,m^{-3}$
n	Exponent in Glen's flow law	3	-
$\dot{\epsilon_0}$	viscosity regularization	10^{-30}	a^{-1}
A_0	Flow law parameter		
	when T $\leq$ 263.15 K	3.985×10^{-13}	$Pa^{-3}\,s^{-1}$
	when T $>$ 263.15 K	1.916×10^{3}	$Pa^{-3}\,s^{-1}$
Q	Creep activation energy		
	when T $\leq$ 263.15 K	60	$kJ\,mol^{-1}$
	when T $>$ 263.15 K	139	$kJ\,mol^{-1}$
R	Universal gas constant	8.31	$J\,mol^{-1}\,K^{-1}$
k	Thermal conductivity	2.1	$W\,m^{-1}\,K^{-1}$
c_p	Heat capacity of ice	2009	$J\,kg^{-1}\,K^{-1}$
L	Latent heat of fusion of ice	3.35×10^{-5}	$J\,kg^{-1}$
T_0	Triple-point temperature of water	273.16	K
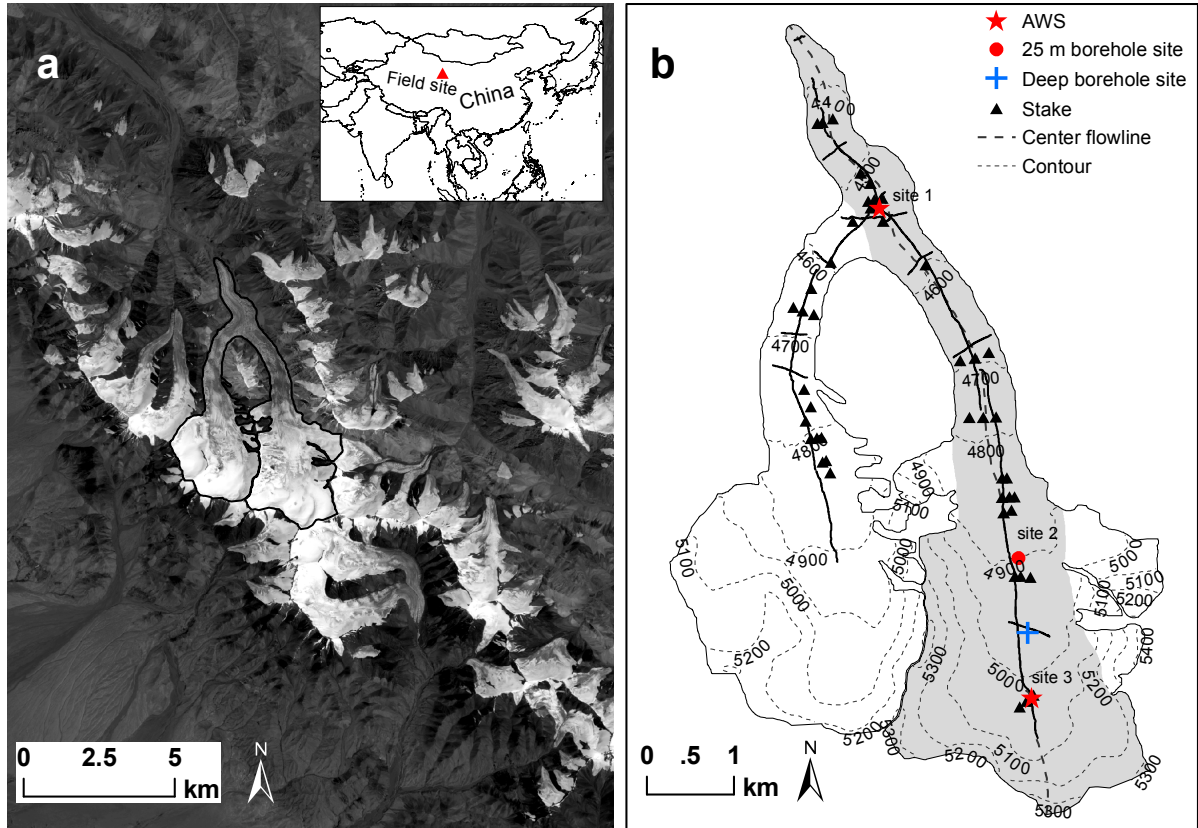
Figure 1. (a) The location of LHG12 in the west Mt. Qilian Shan, China. (b) The solid and thick black lines indicate the GPR survey lines. The shaded area denotes the mainstream of LHG12, which only includes the east branch and neglects the west branch and all small tributaries. The dashed black line represents the center flowline. Red stars indicate the locations of the automatic weather stations and the 25 m deep shallow boreholes (sites 1 and 3). A solid red circle represents the location of the shallow borehole at site 2, and a blue cross represents the location of the deep ice borehole. Black triangles show the positions of the stakes used for ice surface velocity measurements. The contours were generated from SRTM DEM in 2000.
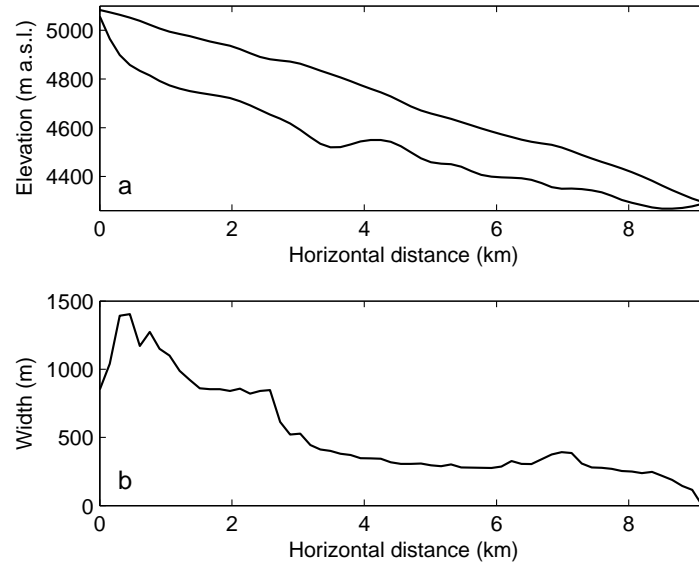
Figure 2. (a) Glacier surface and bed topography along the center flowline. (b) Glacier widths along the center flowline.
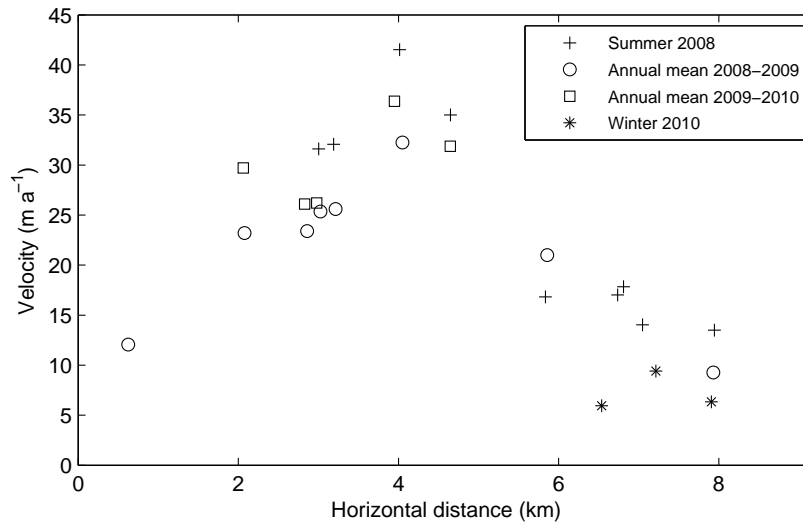

Figure 3. Measured ice surface velocities along the center flowline.
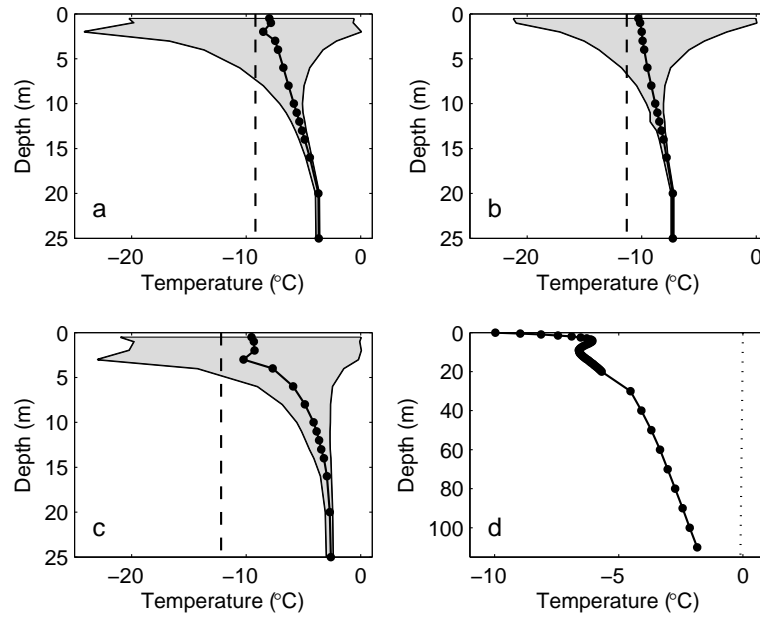
Figure 4. Ice temperature measurements from the four ice boreholes. (a, b, c) Ice temperature measurements from the 25 m deep boreholes at sites 1, 2, and 3, respectively. The black dots show the mean annual ice temperatures over the period of 2010 – 2011. The shaded areas show the yearly fluctuation range of the ice temperature. The dashed lines indicate the mean annual air temperature. (d) Measured ice temperatures from the deep borehole. The dotted line denotes the pressure-melting point (PMP) as a function of elevation.
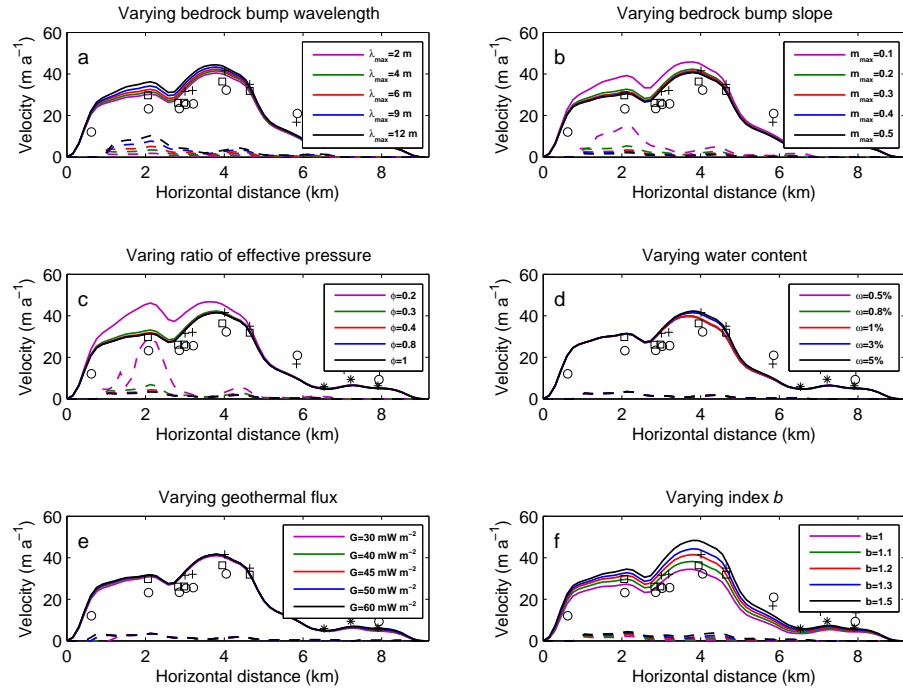
Figure 5. The sensitivity of the modeled ice flow speeds to parameters along the CL. The solid and dashed lines indicate the modeled surface and basal sliding velocities, respectively. Symbols show the measured ice surface velocities (Fig. 3).
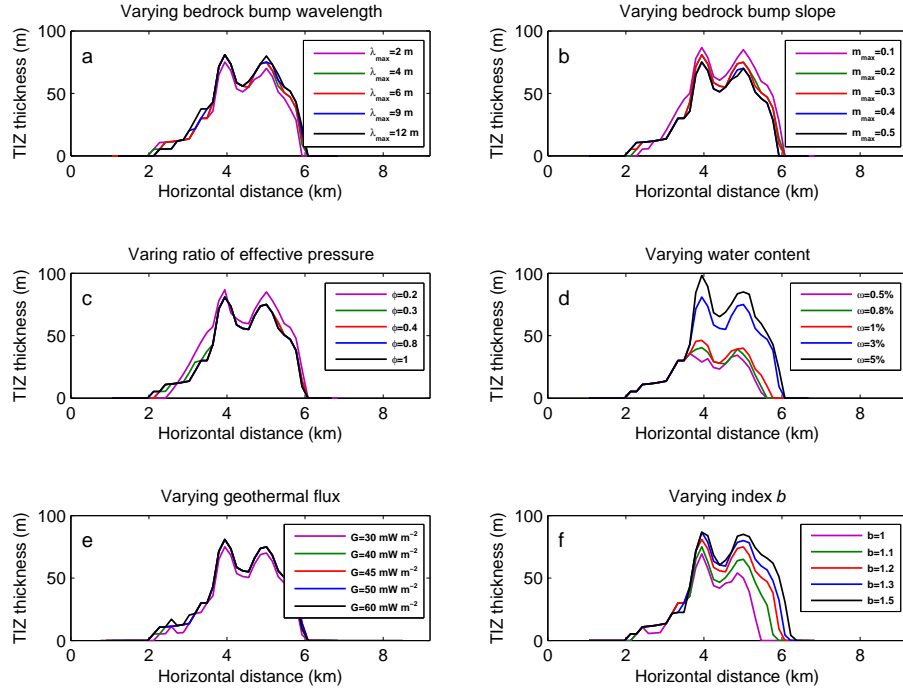
Figure 6. The sensitivity of the modeled temperate ice thicknesses to parameters along the CL. The parameter settings are same as those described in Fig. 5.
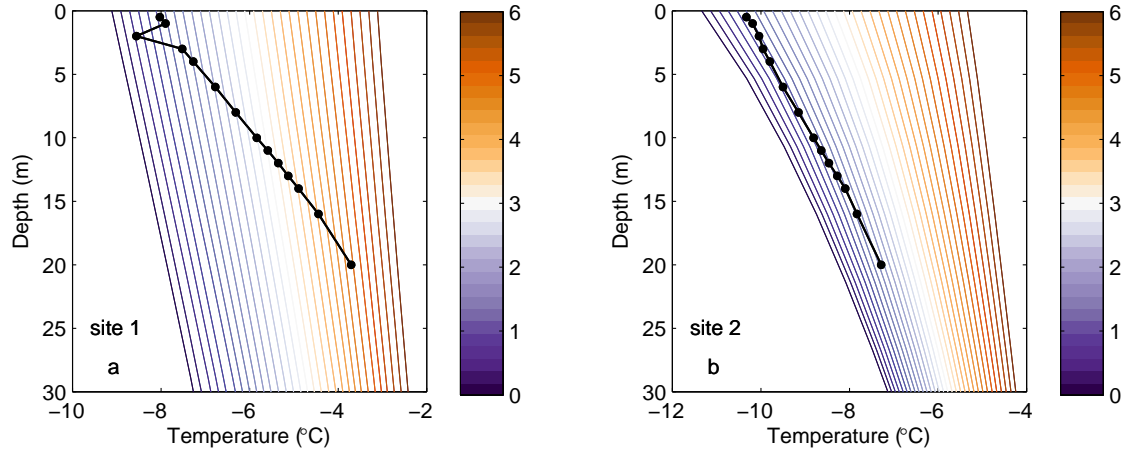

Figure 7. Sensicitity experiments of the tuning parameter c by comparing the measured (black dotted lines) and modeled (coloured lines) 20 m borehole temperatures at sites 1 (a) and 2 (b). The step size of varying the c value is 0.2 K.
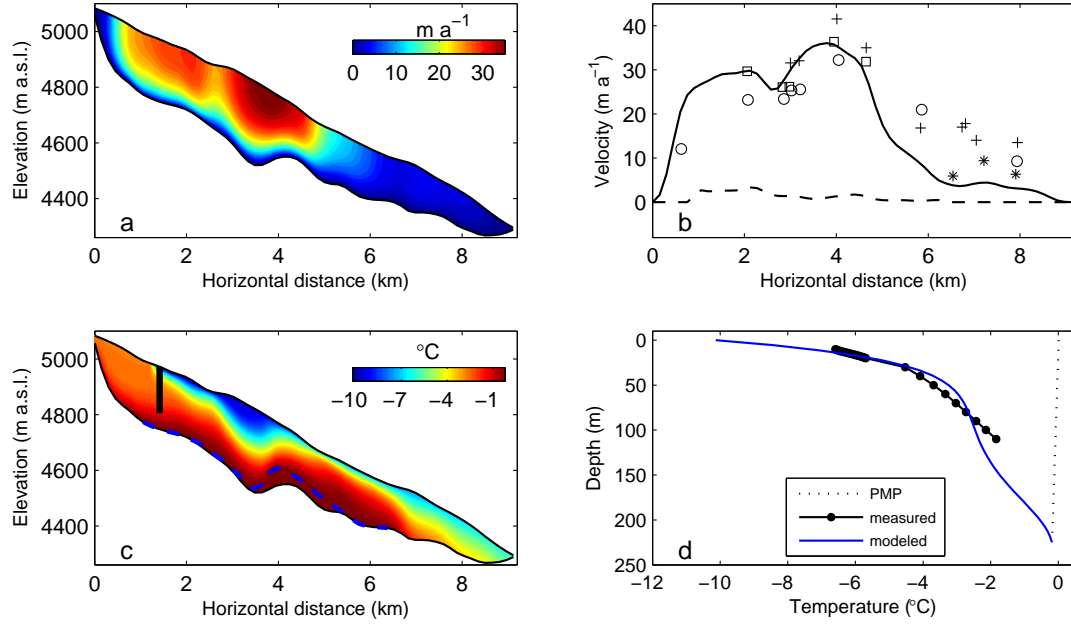
Figure 8. A comparison of the modeled and measured ice temperatures and horizontal velocities (u). (a) The distribution of the modeled horizontal ice velocity (u). (b) Measured (symbols) and modeled (solid line) surface and basal (dashed line) horizontal velocities. The symbols are the same as described in Fig. 3. (c) The distribution of the modeled ice temperature. The blue dashed line indicates the CTS position, and the black bar shows the location of the deep ice borehole. (d) Modeled (blue line) and measured (dots) ice temperature profiles for the deep borehole. The pressure-melting point is shown by the dotted line.
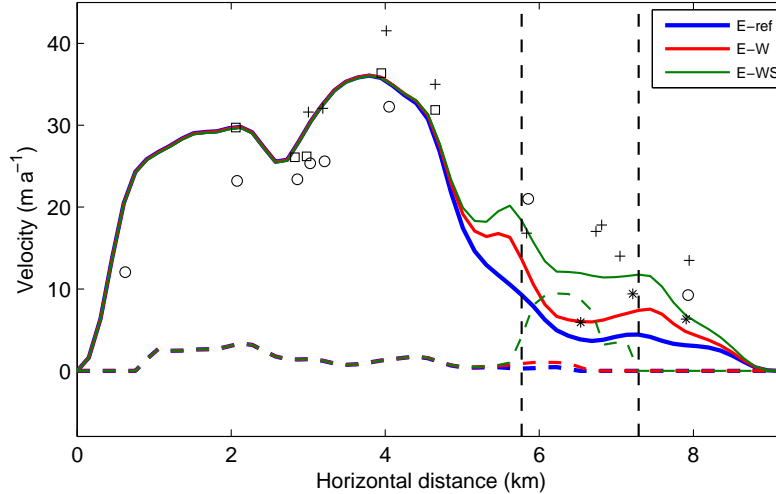
Figure 9. Modeled ice velocities for experiments E-ref (blue line), E-W (red line), and E-WS (green line). The glacier widths in the zone of km 5.8 – 7.3 (bounded by the vertical dashed lines) are increased by 450 m for E-W and E-WS. In E-WS we also include a basal sliding enhancement between km 5.8 – 7.3.
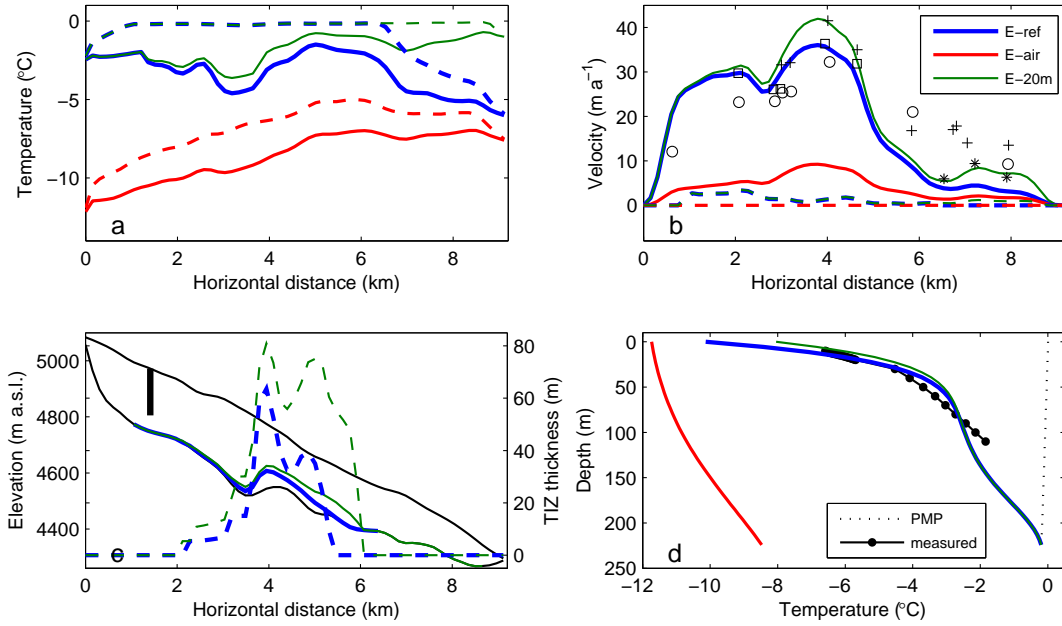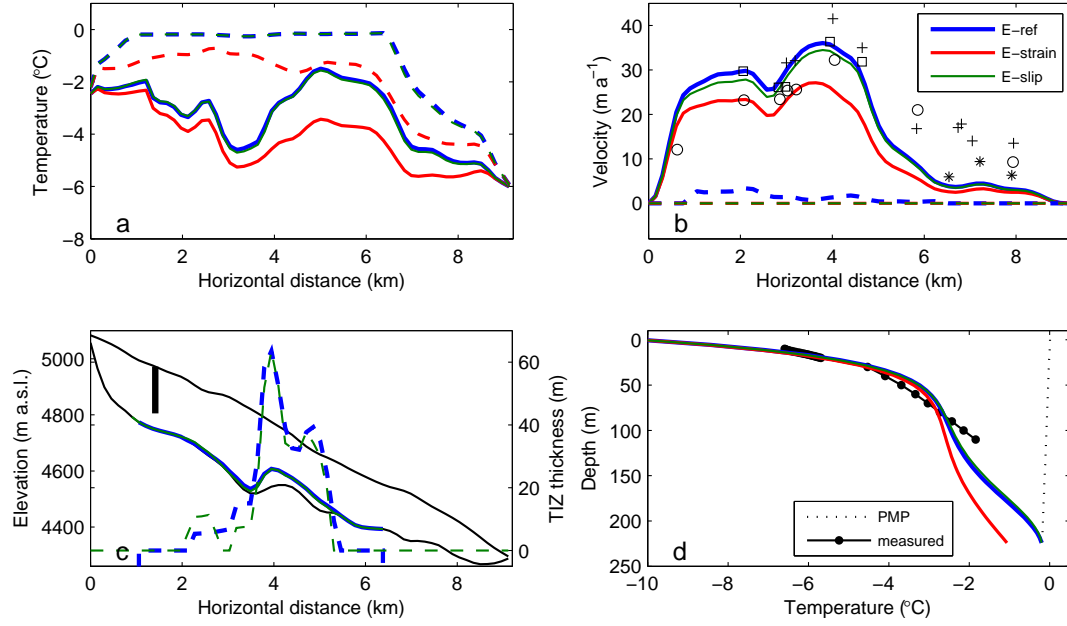
Figure 10. Modeled ice temperatures and velocities for experiments E-ref (blue line), E-air (red line), and E-20m (green line). (a) Modeled column mean (solid lines) and basal (dashed lines) ice temperatures along the CL. (b) Modeled surface (solid lines) and basal (dashed lines) ice velocities along the CL. The symbols for the measured ice surface velocities are the same as those shown in Fig. 3. (c) Modeled CTS position (solid lines) and TIZ thickness (dashed lines). The black bar shows the location of the deep ice borehole. (d) Measured (dots) and modeled (coloured lines) ice temperature profiles for the deep borehole. The dotted line shows the pressure-melting point as a function of ice depth.
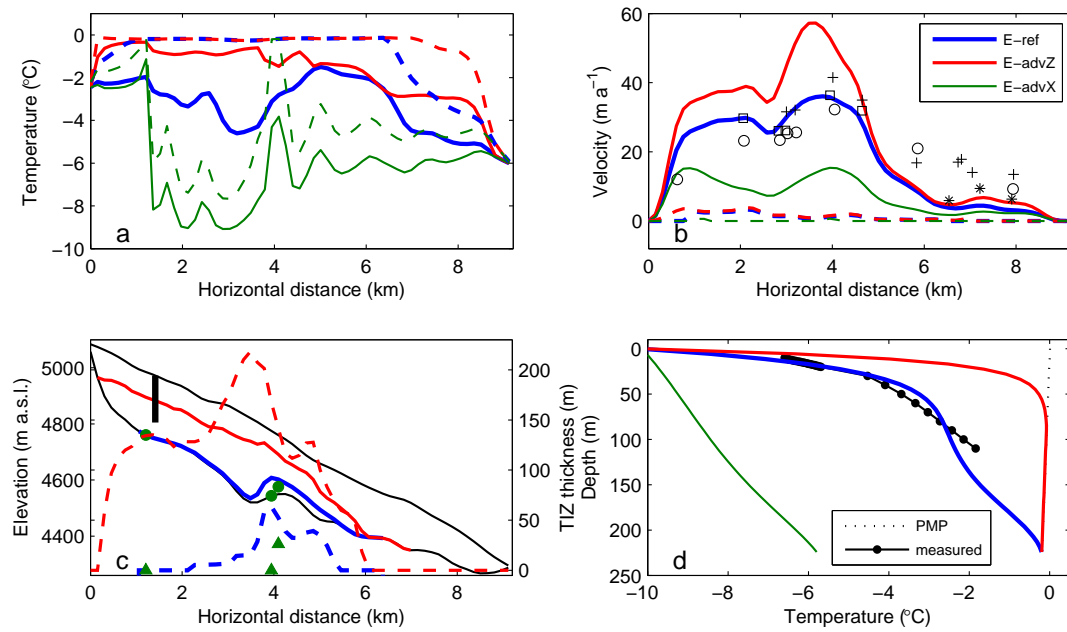
Figure 11. Modeled ice temperatures and velocities for experiments E-ref (blue line), E-advZ (red line) and E-advX (green line). (a) Modeled column mean (solid lines) and basal (dashed lines) ice temperatures along the CL. (b) Modeled surface (solid lines) and basal (dashed lines) ice velocities along the CL. The symbols for the measured ice surface velocities are the same as those shown in Fig. 3. (c) Modeled CTS position (solid lines and filled circles) and TIZ thickness (dashed lines and filled triangles). The filled circles and triangles denote the discontinuous CTS locations and TIZ thicknesses in E-advX, respectively. The black bar shows the location of the deep ice borehole. (d) Measured (dots) and modeled (coloured lines) ice temperature profiles for the deep borehole. The dotted line shows the pressure-melting point as a function of ice depth.

Figure 12. Modeled ice temperatures and velocities for experiments E-ref (blue line), E-strain (green line) and E-slip (purple line). (a) Modeled column mean (solid lines) and basal (dashed lines) ice temperatures along the CL. (b) Modeled surface (solid lines) and basal (dashed lines) ice velocities along the CL. The symbols for the measured ice surface velocities are the same as those shown in Fig. 3. (c) Modeled CTS position (solid lines) and TIZ thickness (dashed lines). The black bar shows the location of the deep ice borehole. (d) Measured (dots) and modeled (coloured lines) ice temperature profiles for the deep borehole. The dotted line shows the pressure-melting point as a function of ice depth.